ARTICLE Open Access

A framework for Frizzled-G protein coupling and implications to the PCP signaling pathways

Zhibin Zhang[1,2], Xi Lin [1], Ling Wei[3], Yiran Wu [1], Lu Xu[1], Lijie Wu[1], Xiaohu Wei [2], Suwen Zhao [1,2], Xiangjia Zhu [3✉] and Fei Xu [1,2,4✉]

Abstract
The ten Frizzled receptors (FZDs) are essential in Wnt signaling and play important roles in embryonic development and tumorigenesis. Among these, FZD6 is closely associated with lens development. Understanding FZD activation mechanism is key to unlock these emerging targets. Here we present the cryo-EM structures of FZD6 and FZD3 which are known to relay non-canonical planar cell polarity (PCP) signaling pathways as well as FZD1 in their G protein-coupled states and in the apo inactive states, respectively. Comparison of the three inactive/active pairs unveiled a shared activation framework among all ten FZDs. Mutagenesis along with imaging and functional analysis on the human lens epithelial tissues suggested potential crosstalk between the G-protein coupling of FZD6 and the PCP signaling pathways. Together, this study provides an integrated understanding of FZD structure and function, and lays the foundation for developing therapeutic modulators to activate or inhibit FZD signaling for a range of disorders including cancers and cataracts.

Introduction

Frizzled proteins (FZDs) are class F G protein-coupled receptors (GPCRs) that mediate Wnt signaling through transducer proteins including Disheveled (DVL) or heterotrimeric G proteins[1]. Dysregulation of these receptors can lead to various human diseases ranging from cancer, developmental defects to metabolic and neurological disorders[2,3]. All FZDs contain a highly conserved cysteine-rich domain (CRD) followed by a flexible linker varying in length in different FZDs and a compact hinge domain before the transmembrane domain[4] (Supplementary Fig. S1a). Unlike most GPCRs, FZD signaling was initially divided into two major pathways, being either dependent (canonical signaling) or independent (non-canonical signaling) on the accumulation of the transcription regulator β-catenin. The two non-canonical signaling pathways are the planar cell polarity (PCP) pathway and the Ca^{2+} pathway[5,6].

Polarity describes structural, biochemical, or functional asymmetry in cells[7]. All mammalian cells experience polarity during their lifespan. There are two types of polarity: the cell intrinsic apical–basal polarity and the tissue wide polarity known as PCP[8]. FZD3/6 and their downstream DVL are known to relay PCP pathways albeit the underlying mechanism is still unknown[9]. On the other hand, the PCP signaling pathway has received increasing attention attributed to its important role in orchestrating oriented cell migration and other polarized cell behaviors that are critical to many developmental processes and disorders[10]. For example, the lens of the eye maintains its polarity and transparency as it grows because it has highly ordered growth patterns such as lens fiber cell elongation, alignment and orientation, which is mediated by the PCP pathway[11,12]. Disorganized lens fiber cell alignment causes cataract[13].

Previous studies have shown that FZD3/6 are also associated with the growth and metastasis of various cancers, through mediating the non-canonical signaling

Correspondence: Xiangjia Zhu (zhuxiangjia1982@126.com) or Fei Xu (xufei@shanghaitech.edu.cn)
[1]iHuman Institute, ShanghaiTech University, Shanghai, China
[2]School of Life Science and Technology, ShanghaiTech University, Shanghai, China
Full list of author information is available at the end of the article
These authors contributed equally: Zhibin Zhang, Xi Lin, Ling Wei

pathways[14]. For instance, migration of breast cancer cells can be inhibited through the FZD3-dependent cAMP signaling pathway[15]; FZD6 is involved in human neuroblastomas in a β-catenin-independent manner[16]. Additionally, FZD1 also participates in cancer development and progression, such as colon cancer[17].

Despite their important roles in cancer and other human diseases, no successful drugs have been developed for any of the ten FZDs. Previous drug discovery efforts have been focused on the anti-FZD antibody by blocking Wnt–FZD interactions but the efficacy and target selectivity is so far limited. Structural insights to elucidate the receptor activation mechanism would be valuable for probing the drug intervention hotspots and guiding the design of new tool ligands for the FZDs. Recently, Xu et al. reported the first structure of FZD and G protein complex providing structural insight into a constitutively active state of the FZD7[18]. FZD1, FZD3 and FZD6 are reported to couple to G proteins as well, but the conclusion is vague[15,19]. Indeed, there are three gaps in our understanding of FZD signal transduction that need to be addressed: whether G protein is coupled to each FZD and which subtype; the relationship between G protein coupling and downstream signaling pathways; and whether there is a conserved activation mechanism, such as molecular switches, that is shared by all FZDs. Here we report the cryo-electron microscopy (cryo-EM) structures for FZD1, FZD3 and FZD6, including three structures in G protein-coupled and active states, and three structures in G protein-free and inactive states. The inactive/active structure pairs showed characteristic activation mechanisms of FZDs that are distinct from other GPCRs. Our study also investigated the potential crosstalk between PCP pathway and the G protein activation of FZD6, which provides a novel understanding of the FZD signal transduction. These comprehensive understandings of the structural and functional landscape of FZDs will provide an opportunity for developing structure-based tool ligands for FZDs' signaling investigation.
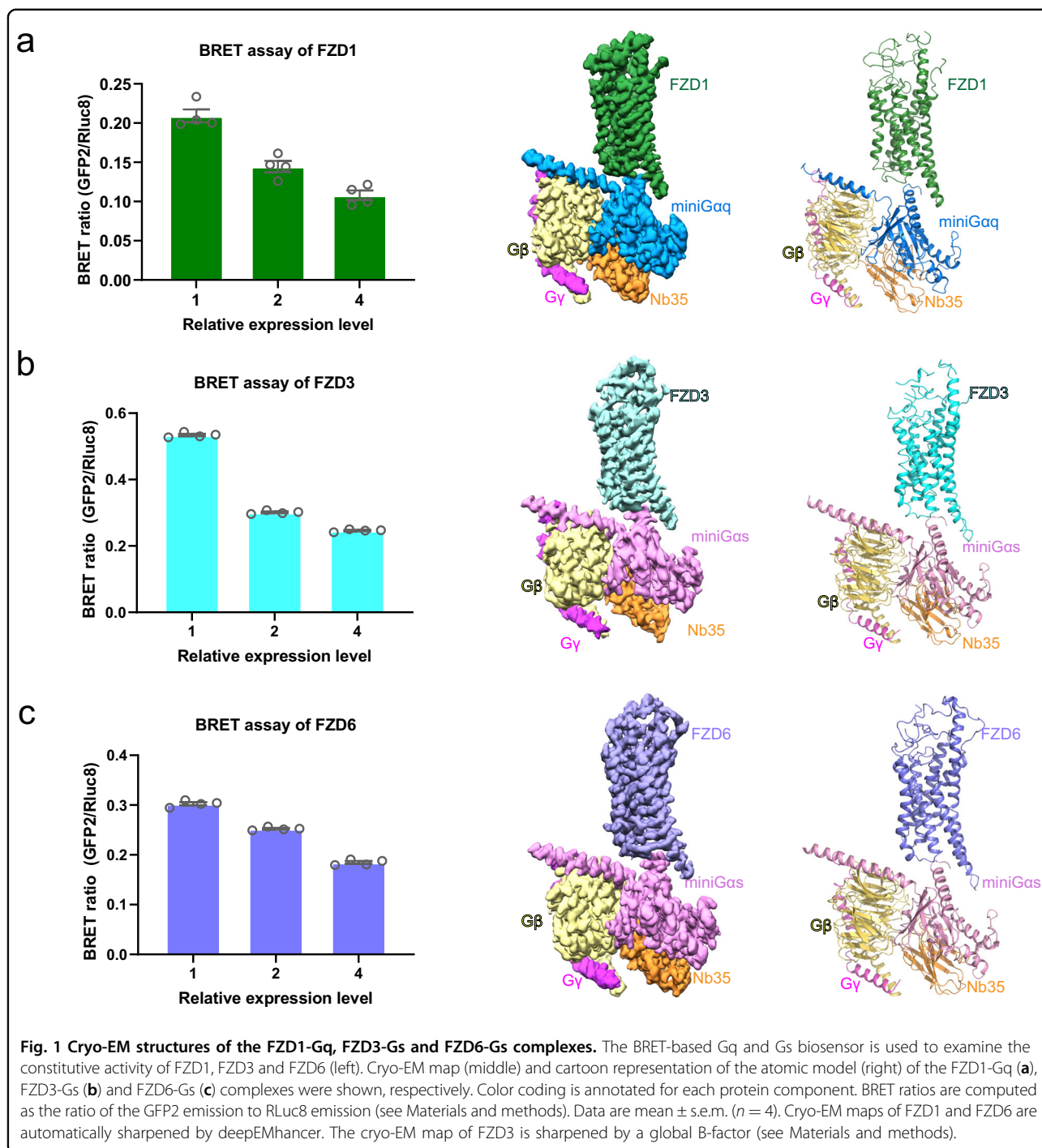
Results

Three constitutively active FZDs

FZDs are classified as non-classical GPCRs with multi-domain topology and mediating signaling pathways through DVL and other transducers[20,21] (Supplementary Fig. S1a). Previous studies showed that FZD7 can engage Gs in a ligand-free (apo) state[18], it remains to be seen whether FZD1, FZD3 and FZD6 can signal through heterotrimeric G proteins in the absence of an agonist. To understand the downstream G protein subtypes for FZD1, FZD3 and FZD6, we first developed bioluminescence resonance energy transfer assay (BRET2) to evaluate the constitutive activity of three

FZDs' signaling in major Gα subunits — Gq, Gi1, Gs, G12, Gi2, Gi3, GoA, GoB, GZ, GGust, G11, G13 and G15[22]. This assay can detect the dissociation of heterotrimeric G proteins, which is the proximal step when the G protein signaling cascades are initiated, and it has been widely used in direct measurements of receptor-transducer coupling[23]. According to the results, we found that all the three FZDs exhibited constitutive activity in G protein recruitment, in which FZD1 has a constitutive Gq activity (Fig. 1a; Supplementary Fig. S2a), while both FZD3 and FZD6 have constitutive Gs activities (Fig. 1b, c; Supplementary Fig. S2b, c). In addition, FZD6 also exhibited a relatively high constitutive activity in G12 signaling (Supplementary Fig. S2c). Therefore, we assembled FZD1-Gq, FZD3-Gs and FZD6-Gs complexes for structural studies aiming to elucidate the G protein binding framework for FZDs.
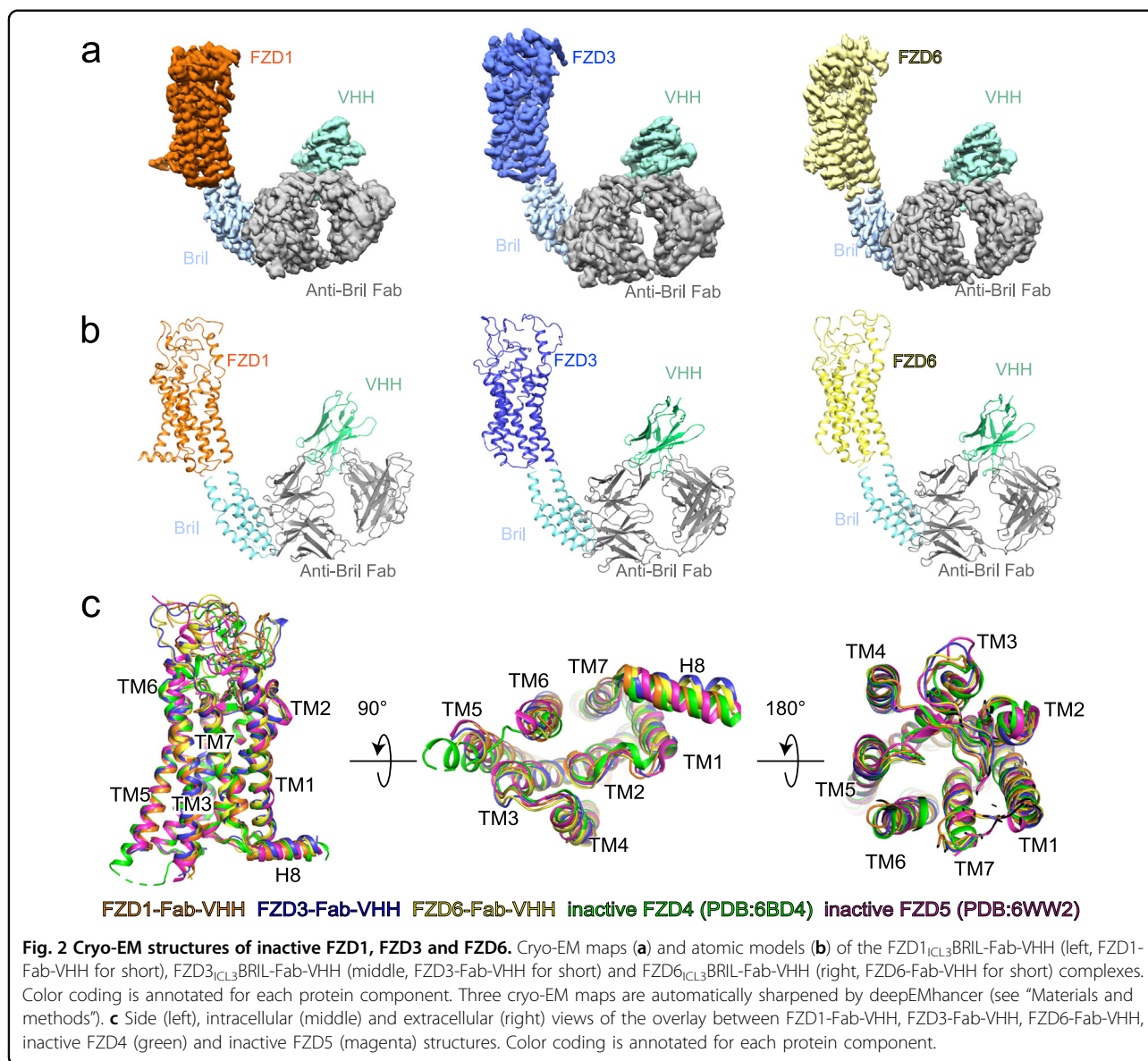
Structures of FZD-G protein complexes

To obtain stable FZD-G Protein complex for structural investigation, we assembled purified FZD proteins with mini-Gα[24], Gβ1γ2 and the camelid antibody 35 (Nb35). Size-exclusion chromatography (SEC) and SDS-PAGE analysis reveal that purified FZD1 can form a monodispersed complex with mini-Gq (Gq); both FZD3 and FZD6 can form stable complex with mini-Gs (Gs) (Supplementary Figs. S3–S5). The structures of FZD1-Gq, FZD3-Gs and FZD6-Gs complexes were finally determined at a global resolution of 3.6 Å, 3.5 Å and 3.4 Å, respectively, by cryo-EM single particle analysis (Fig. 1a–c; Supplementary Figs. S3–S5). The cryo-EM maps are sufficiently clear to trace the position of the receptor, the G protein trimer and the Nb35 (Fig. 1a–c; Supplementary Figs. S3–S5). No density of CRD is observed because of its flexible connection through a disordered linker with the transmembrane domain. This is consistent with our previous observation with the FZD7-Gs complex[18]. The overall structure of FZD1 consists of a hinge domain (HD, residues 275–312), the transmembrane domain (TM, residues 313–622) and an amphipathic helix (H8) (Fig. 1a; Supplementary Fig. S1b). FZD3 and FZD6 also contain the HD and TM domains but lack the H8 (Fig. 1b, c; Supplementary Fig. S1b). The overall structures of three FZD-G protein complexes are similar with the canonical GPCR-G protein complexes. Structural comparison of FZD1-Gq, FZD3-Gs and FZD6-Gs with active and inactive SMO (PDB: 6OT0[25] and 4JKV[26], respectively) reveals an outward movement of TM6 in these three new FZD-G protein complexes relative to inactive SMO. Such a movement of TM6 was also observed in the FZD7-Gs (PDB: 7EVW[18]) previously, suggesting that these three FZD-G protein complexes (FZD1-Gq, FZD3-Gs and FZD6-Gs) are all in active states (Supplementary Fig. S6a, b).

Fig. 1 Cryo-EM structures of the FZD1-Gq, FZD3-Gs and FZD6-Gs complexes. The BRET-based Gq and Gs biosensor is used to examine the constitutive activity of FZD1, FZD3 and FZD6 (left). Cryo-EM map (middle) and cartoon representation of the atomic model (right) of the FZD1-Gq (**a**), FZD3-Gs (**b**) and FZD6-Gs (**c**) complexes were shown, respectively. Color coding is annotated for each protein component. BRET ratios are computed as the ratio of the GFP2 emission to RLuc8 emission (see Materials and methods). Data are mean ± s.e.m. ($n = 4$). Cryo-EM maps of FZD1 and FZD6 are automatically sharpened by deepEMhancer. The cryo-EM map of FZD3 is sharpened by a global B-factor (see Materials and methods).

Structures of three FZDs in the inactive state

To better understand the conformational changes during FZDs' activation, we solved the structures of FZD1, FZD3 and FZD6 without G-protein heterotrimers. FZDs with a thermostabilized *Escherichia coli* apocytochrome *b*562RIL (BRIL)[27] fused in ICL3, anti-BRIL Fab and anti-Fab VHH are expressed and purified separately and assembled into complexes in vitro[28].

Finally, the structures of anti-BRIL Fab bound FZD1, FZD3 and FZD6 (FZD1-Fab-VHH, FZD3-Fab-VHH and FZD6-Fab-VHH) were determined at a global resolution of 3.5 Å, 3.4 Å and 3.3 Å, respectively (Fig. 2a; Supplementary Figs. S3–S5). These density maps allowed us to trace the polypeptide chains and build the atomic structures of three FZDs from the hinge domain to H8, except ICL3 due to the replacement of BRIL (Fig.

Fig. 2 Cryo-EM structures of inactive FZD1, FZD3 and FZD6. Cryo-EM maps (**a**) and atomic models (**b**) of the FZD1$_{ICL3}$BRIL-Fab-VHH (left, FZD1-Fab-VHH for short), FZD3$_{ICL3}$BRIL-Fab-VHH (middle, FZD3-Fab-VHH for short) and FZD6$_{ICL3}$BRIL-Fab-VHH (right, FZD6-Fab-VHH for short) complexes. Color coding is annotated for each protein component. Three cryo-EM maps are automatically sharpened by deepEMhancer (see "Materials and methods"). **c** Side (left), intracellular (middle) and extracellular (right) views of the overlay between FZD1-Fab-VHH, FZD3-Fab-VHH, FZD6-Fab-VHH, inactive FZD4 (green) and inactive FZD5 (magenta) structures. Color coding is annotated for each protein component.
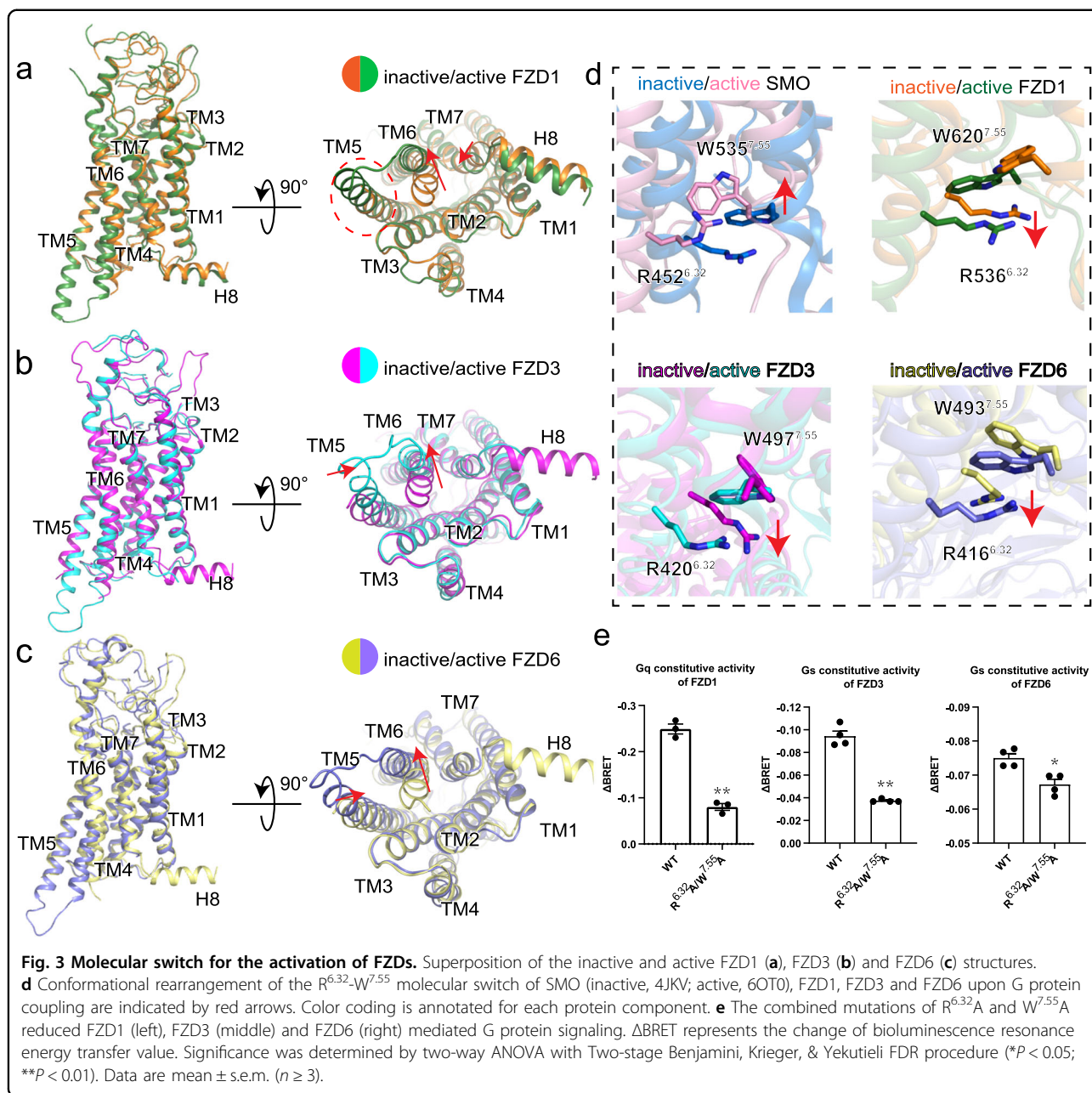
2b). The CRD domain is still disordered and unmodeled in these structures, indicating that the CRD domain is flexible in both G-protein coupled and apo inactive FZDs. Through comparison of FZD1-Fab-VHH, FZD3-Fab-VHH and FZD6-Fab-VHH with inactive FZD4 (PDB: 6BD4[4]) and inactive FZD5 (PDB: 6WW2[29]) as well as active and inactive SMO, we found that these three FZD-Fab-VHH complexes were captured in an inactive state resembling the conformation of the inactive FZD4, inactive FZD5 and inactive SMO structures (Fig. 2c; Supplementary Fig. S6c). Thus, we conclude that these three FZD-Fab-VHH complexes (FZD1-Fab-VHH, FZD3-Fab-VHH and FZD6-Fab-VHH) are all in apo inactive states.

Activation mechanism of FZDs

To understand the activation mechanism of FZDs, we compared each inactive-state FZD with its respective active-state structure. Structural comparison of FZD-G protein complexes and FZD-Fab-VHH complexes reveals an outward movement in TM6 at the cytoplasmic side in the G protein-coupled relative to G protein-free states. In addition, an inward shift of TM7 in FZD1 and inward shift of TM5 in FZD3 and FZD6 were observed at the cytoplasmic side in the FZD-G protein complexes (Fig. 3a–c).

W[7.55] and R[6.32] have been proposed to serve as a conserved molecular switch in class F receptors including SMO[21]. For SMO, previous study suggested a weakened but preserved π-cation interaction between W[7.55] and

Fig. 3 Molecular switch for the activation of FZDs. Superposition of the inactive and active FZD1 (**a**), FZD3 (**b**) and FZD6 (**c**) structures. **d** Conformational rearrangement of the $R^{6.32}$-$W^{7.55}$ molecular switch of SMO (inactive, 4JKV; active, 6OT0), FZD1, FZD3 and FZD6 upon G protein coupling are indicated by red arrows. Color coding is annotated for each protein component. **e** The combined mutations of $R^{6.32}A$ and $W^{7.55}A$ reduced FZD1 (left), FZD3 (middle) and FZD6 (right) mediated G protein signaling. ΔBRET represents the change of bioluminescence resonance energy transfer value. Significance was determined by two-way ANOVA with Two-stage Benjamini, Krieger, & Yekutieli FDR procedure (*$P < 0.05$; **$P < 0.01$). Data are mean ± s.e.m. ($n \geq 3$).

$R^{6.32}$ after Gi coupling[25]. For FZDs, this molecular switch was not mentioned in the inactive FZD4 structure[4]; subsequent research proposed that this π-cation interaction in inactive FZD5 might be more extensive than that in FZD4 (Supplementary Fig. S7h)[29]; structural analysis and molecular dynamics studies of the FZD7-G protein complex suggested that the dynamic interaction between $W^{7.55}$ and $R^{6.32}$ might play a role in the receptor's activation[18]. All previous conclusions are vague due to the lack of inactive/active pair for the same receptor: FZD4 and FZD5 only have inactive structures while FZD7 only has active structure. Here we compared the inactive-to-

active structural transformations for FZD1/3/6 by taking advantage of their structures in both functional states reported in this study. Through structural alignment of inactive/active structures of FZD1/3/6, a consistently downward movement of $W^{7.55}$ was observed while the three FZDs were activated (Fig. 3d). However, $W^{7.55}$ in SMO shows an upward movement upon activation (Fig. 3d). Despite conformational changes, the strong π-cation interaction between $W^{7.55}$ and $R^{6.32}$ persists in the active structures for FZD1/3/6 (Supplementary Fig. S7a–c). The combined alanine mutations of $W^{7.55}$ and $R^{6.32}$ reduced the basal signaling activity of FZD1/3/6, implying the

importance of this molecular switch for FZDs' activation (Fig. 3e). It is noteworthy that a comprehensive structural comparison with GPCRs in other classes revealed that this molecular switch was not found in representative receptors from other classes including β_2AR[30,31] in class A, GLP-1R[32,33] in class B, and mGlu4[34] in class C (Supplementary Fig. S7d).

Another two conserved structural features were found by careful alignment of inactive/active pairs for each FZD: kink $P^{6.43}$ and the $W^{3.43}$–$Y^{6.40}$ interaction. The outward movement of TM6 in all three FZDs begins at $P^{6.43}$, which together with $I^{7.47}$ and $V^{7.48}$ forms a hydrophobic network between TM6 and TM7. When the receptor is activated, $P^{6.43}$ kinks away from $I^{7.47}$ and $V^{7.48}$ and triggers the movement of TM6 at the cytoplasmic end (Supplementary Fig. S7e). Sequence alignment shows that $P^{6.43}$, I/V/L$^{7.47}$ and $V^{7.48}$ are conserved in all ten FZDs (Supplementary Fig. S7j), indicating a family-characteristic motif related to activation of FZDs. Mutation of P547$^{6.43}$A in FZD1 which abolished its ability to kink decreased the Gq signaling for FZD1 (Supplementary Fig. S8a). Similarly, mutation of P431$^{6.43}$A in FZD3 and P427$^{6.43}$A, I485$^{7.47}$G, V483$^{7.48}$G in FZD6 also impaired the basal activity in Gs signaling (Supplementary Fig. S8c, e). The $W^{3.43}$–$Y^{6.40}$ interaction pair was also found important for FZD activation. When coupled to the G proteins, W420$^{3.43}$ in TM3 of FZD1 moves from TM5 (inactive state) to TM6 (active state) to interact with Y544$^{6.40}$. Such a movement of $W^{3.43}$ was also observed in FZD3 but weakened in FZD6 (Supplementary Fig. S7g). The combined alanine mutations of $W^{3.43}$ and $Y^{6.40}$ reduced the basal signaling activity of FZD1 and FZD3; while no significant decrease was observed in FZD6 consistent with the structural findings (Supplementary Fig. S8a, c, e). The conformational features of these two activation motifs (kink $P^{6.43}$ and the $W^{3.43}$-$Y^{6.40}$ interaction) are conserved in the inactive FZD4, inactive FZD5 and active FZD7 structures (Supplementary Fig. S7f, h) and shared by the other FZDs according to the sequence alignment (Supplementary Fig. S7j). However, the sequences of these two motifs are not conserved in SMO further indicating that SMO and FZDs may employ different activation mechanisms (Supplementary Fig. S7j).
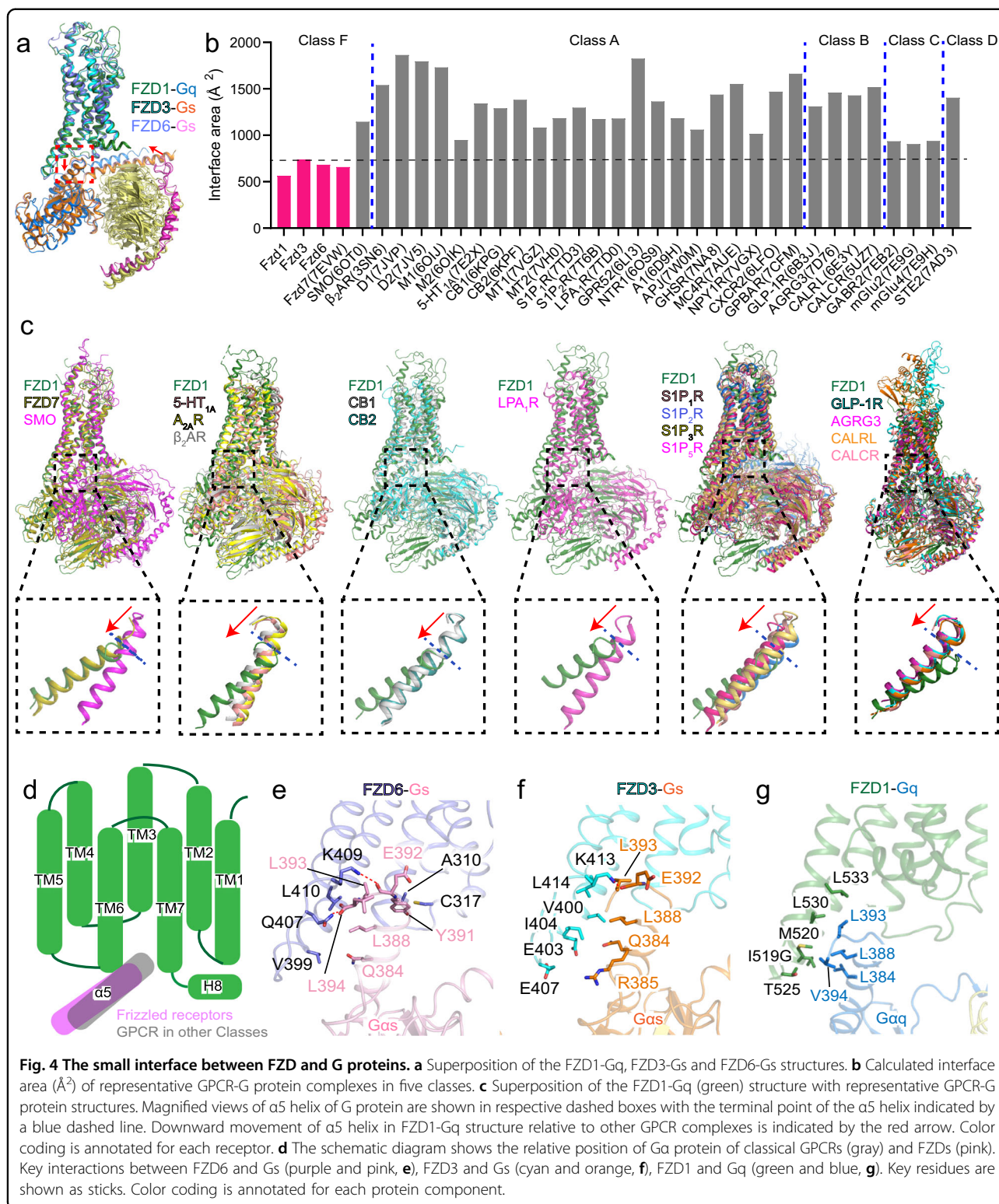
Since some SMO variants also exhibit constitutive activity, such as D384R, D473R[35], and G111C/I496C[36], we compared FZD-G protein structures to those of constitutively active SMO variants. In contrast to the D384R mutation in SMO, which leads to steric hindrance, trapping sterols within the 7TMs to trigger the Hedgehog signal, the corresponding residue at this position in FZD1, FZD3, and FZD6 is aspartic acid, and this would not induce a similar structural effect as that of D384R (Supplementary Fig. S6d). While for the G111C/I496C variant, a newly formed disulfide bond would induce a conformational change leading to SMO activation. However, no corresponding residues in this region were found in FZDs (Supplementary Fig. S6e). These comparisons indicate different mechanisms between constitutive FZD1, FZD3, FZD6 and constitutive SMO variants.

The small interface between FZDs and G proteins

Previous structural analysis showed a very small interface between FZD7 and Gs in the FZD7-Gs complex structure[18], which prompted us to examine the G protein engagement in the three FZD-G protein complexes reported in this study. First, we calculated the interface area of several representative GPCR-G protein complexes and found that the four FZDs—FZD1, FZD3, FZD6, and FZD7 have the smallest G protein interface compared to receptors in other representative classes (Fig. 4a, b). It is noteworthy that the G protein interface area in SMO is about twice of FZDs (Fig. 4b), which further illustrates that SMO is different from FZDs in their activation mechanisms. Next, we compared the overall structure of FZD1-Gq complex with several representative GPCR-G protein complexes, including β_2 adrenergic receptor (β_2AR)[37], adenosine A$_{2A}$ receptor (A$_{2A}$R)[38], serotonin receptor (5-HT$_{1A}$)[39], cannabinoid receptors (CB1 and CB2)[40], lysophosphatidic acid receptor (LPA$_1$R)[41], sphingosine 1-phosphate receptors (S1P$_1$R, S1P$_2$R, S1P$_3$R and S1P5R)[41–44] in class A, glucagon-like peptide-1 receptor (GLP-1R)[45] and calcitonin gene-related peptide receptor (CALRL)[46], the calcitonin receptor (CALCR)[47] in class B1, and adhesion receptor AGRG3[48] in class B2, and found that the position of the αH5 in FZD1 is at least one helix lower than that in other GPCRs when we align on the receptor side (Fig. 4c, d).

The overall G protein engagements of FZD3/6 are similar, which are mainly mediated by the hydrophobic interactions, polar interactions, and hydrogen bonds between αH5 of Gαs and TM5, TM6 and ICL3 of the receptor. In FZD6-Gs complex, L410$^{6.26}$ forms major hydrophobic interactions with L388$^{G.H5.20}$ and L393$^{G.H5.25}$ (the generic numbering of GPCR database for Gα subunit[49]), C317$^{4.35}$ makes hydrophobic contact with Y391$^{G.H5.23}$, while the side chain of Q407$^{6.23}$ and K409$^{6.25}$ form hydrogen bonds with the carboxyl group of L394$^{G.H5.26}$ and E392$^{G.H5.24}$ (Fig. 4e). In FZD3-Gs complex, V400$^{5.72}$, I404$^{5.76}$ and L414$^{6.26}$ form a triangular, hydrophobic core to interact with Q384$^{G.H5.16}$, L388$^{G.H5.20}$ and L393$^{G.H5.25}$. The side chain of K413$^{6.25}$ forms a hydrogen bond with the carboxyl group of E392$^{G.H5.24}$; E403$^{5.75}$ and E407^{ICL3} of FZD3 form polar interactions with Q384$^{G.H5.16}$ and R385$^{G.H5.17}$ of αH5 (Fig. 4f). Most of the residues that interact with Gs are conserved in FZDs, except C317 of FZD6, as well as E403 and E407 of FZD3 (Supplementary Fig. S9). Consistent with

Fig. 4 The small interface between FZD and G proteins. a Superposition of the FZD1-Gq, FZD3-Gs and FZD6-Gs structures. **b** Calculated interface area (Å²) of representative GPCR-G protein complexes in five classes. **c** Superposition of the FZD1-Gq (green) structure with representative GPCR-G protein structures. Magnified views of α5 helix of G protein are shown in respective dashed boxes with the terminal point of the α5 helix indicated by a blue dashed line. Downward movement of α5 helix in FZD1-Gq structure relative to other GPCR complexes is indicated by the red arrow. Color coding is annotated for each receptor. **d** The schematic diagram shows the relative position of Gα protein of classical GPCRs (gray) and FZDs (pink). Key interactions between FZD6 and Gs (purple and pink, **e**), FZD3 and Gs (cyan and orange, **f**), FZD1 and Gq (green and blue, **g**). Key residues are shown as sticks. Color coding is annotated for each protein component.

the structural findings, mutagenesis and cellular functional assay showed that most of the mutations at the interface reduced the Gs signaling activity of FZD3/6 (Supplementary Fig. S8d, f).

The Gq engagement of FZD1 is mainly mediated by the hydrophobic interactions. $I519^{5.75}$, $M520^{5.76}$, $T525^{ICL3}$, $L530^{6.26}$ and $L533^{6.29}$ of FZD1 form hydrophobic interactions with $L384^{G.H5.16}$, $L388^{G.H5.20}$, $L393^{G.H5.25}$,

$V394^{G.H5.26}$ of αH5, which results in the smallest receptor-G protein interface in the known G protein coupled FZDs structures (Fig. 4g). Mutations of I519G, M520A and L530E on the receptor side caused a reduced Gq signaling activity, indicating the importance of these hydrophobic interactions between receptor and Gq protein (Supplementary Fig. S8b).

Structural findings from the three pairs of FZD structures reported in this study shed light on a framework of FZD-G protein coupling and structural basis of the FZD activation mechanism. The small interface with a cluster of hydrophobic interactions is a representative feature for FZD1/3/6-G protein complexes, and most of the interacting residues on the interface are highly conserved among ten FZDs (Supplementary Fig. S9).

Functional assessments of FZD6/PCP signaling in human lens tissue

Next we aimed to explore how the FZD-G protein signaling axis participates in the broader Wnt signaling pathways. Both FZD3 and FZD6 were known to signal through the PCP/tissue polarity system, but the reported FZD3 phenotype is limited to the nervous system[3] while FZD6 expresses more broadly, including epidermal derivatives[50], lateral ventricular[51], neural tissues[52], etc. The lens of the eye develops polarization structures through the highly coordinated behavior of its cells, making it an ideal model tissue for the study of the PCP pathway. The epithelial cells proliferate and their progeny migrate below the equator of the lens where they elongate and differentiate into secondary fiber cells, in which the FZD6-mediated PCP pathway plays an important role[11,53,54].

We therefore performed the mutagenesis and functional assay in the human lens epithelial cell line SRA 01/04. We selected representative mutations in the FZD6-Gs interface (C317A and Q407A, separately) as well as activation switches ($R^{6.32}A/W^{7.55}A$ combined mutation) for the assessment. Through TOPFlash (canonical β-catenin pathway) and ATF2-based (PCP pathway) luciferase reporter assays, we found that these residues are essential for the PCP pathway but not the canonical pathway (Fig. 5a). This implies that FZD6 may regulate the downstream PCP signaling through activating G proteins. To confirm this result, we also examined the expression levels of downstream factors of the PCP pathway, including Ras Homolog Family Member A (RHOA) and c-Jun N-terminal kinases (JNK). Quantitative RT-PCR assay revealed that all three mutations of FZD6 reduced the expression levels of RHOA, without altering the expression level of the FZD6 gene and the downstream Gαs (GNAS) gene (Fig. 5b). Western blot analysis also indicated that these mutations impaired PCP signaling by reducing the protein expressions of RHOA and phospho-JNK. These decreases were not caused by changes in the

expression of FZD6 or its downstream effector Gαs, suggesting the activation of PCP/RHOA and PCP/JNK pathways were affected by FZD6-Gs complex structural integrity (Fig. 5c).

We then explored how the FZD-G protein signaling axis affects the lens fiber differentiation and polarized cell behaviors using primary culture of human lens epithelial explant. The human lens epithelial cell proliferates, migrates, differentiates and achieves proper fiber cell morphology and alignment throughout the lifetime of an individual to retain a high level of light transmission. These processes can be observed by treating human lens epithelial explants with FGF-2 to induce fiber differentiation, followed by transfection with wild type FZD6 (WT) or FZD6-Gs interface mutation C317A (Fig. 5d). Immunofluorescent staining of F-actin indicated that the cells migrated from the rim of the capsule were highly oriented with well-organized alignment in the WT group, while those cells were less-organized and oriented diversely in the mutation group (Fig. 5e). Furthermore, the WT group showed cytoskeleton rearrangement with isotropic actin filaments, but the mutation group showed disordered cytoskeleton structure with anisotropic actin filaments (Fig. 5e). The surface expression of FZD6 was verified in both SRA 01/04 cell line and human lens epithelial explant after transfection of WT FZD6 and C317A mutation, and no significant difference in the mean fluorescence intensity was observed between the two groups (Supplementary Fig. S10).

Collectively, functional assessment of the FZD-G protein signaling axis indicated the G protein signaling mediated by FZD6 might be essential in activation of PCP signaling in regulating lens cell elongation and polarization.

Discussion

FZDs have been long sought after as emerging targets for a range of cancers and developmental disorders, but so far no drugs have been successfully developed. Understanding the activation mechanisms of the FZDs is vital to unlock the receptor hotspots for drug interventions. However, structural and functional studies for the FZDs have been challenging for several reasons including the low expression and poor stability of the WT FZD proteins, the difficulty of Wnt purification, and whether or not G protein would bind or which subtype. Past studies on FZDs and other GPCRs mainly focus on one conformational state such as active or inactive, while the pairwise comparison of different conformations on one receptor is lacking even with the aid of alphafold. In this study, we first employed BRET2 assay to determine the FZD1/3/6 basal activity in coupling to their respective G protein subtypes. Next, through diligent screening of various constructs, we

Fig. 5 (See legend on next page.)
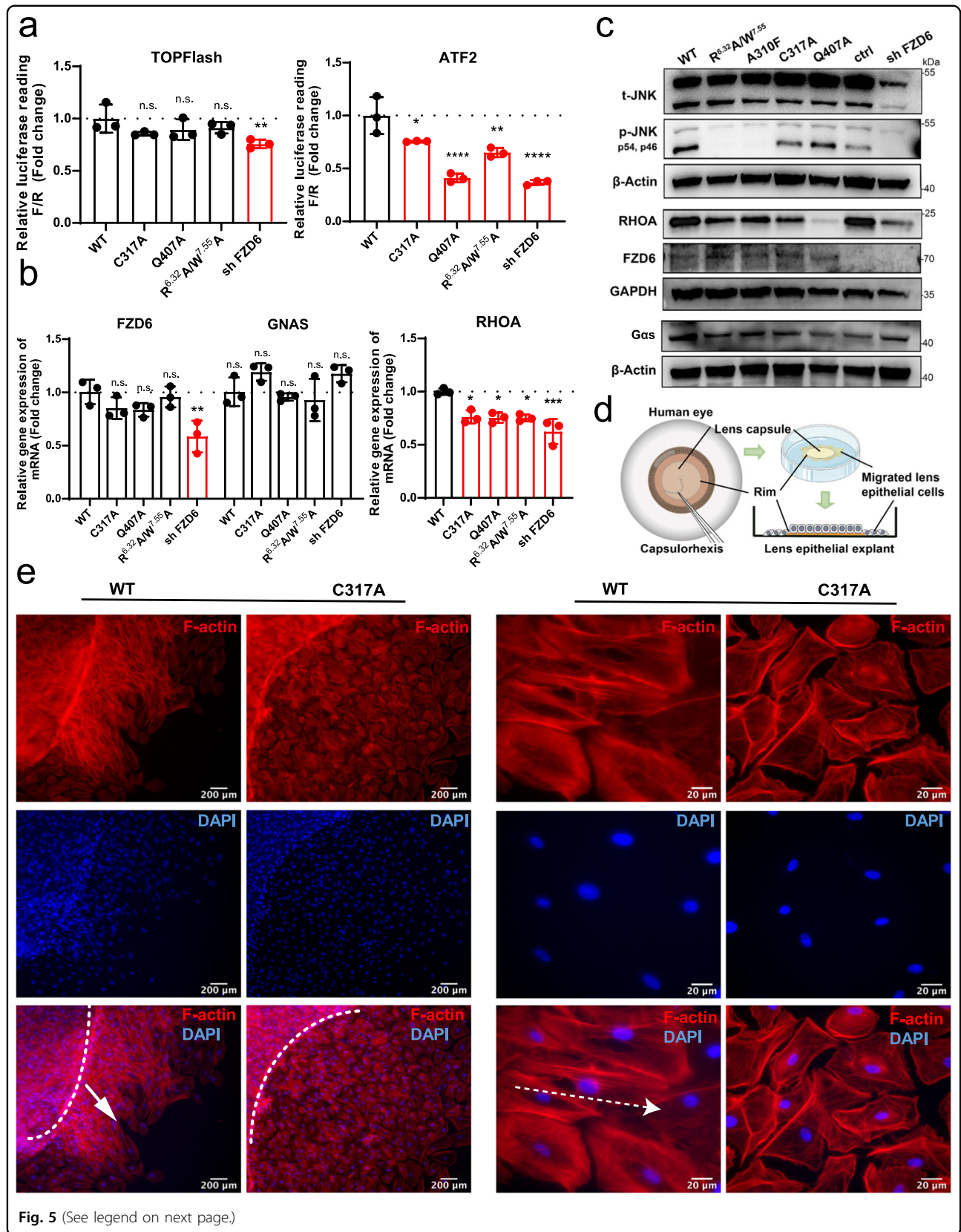
(see figure on previous page)

Fig. 5 Functional assessments of mutations on FZD6 signaling pathways in lens tissue. a Relative TOPFlash and ATF2-luc reporter activity in SRA 01/04 cells transfected with control wild-type (WT) FZD6, the indicated FZD6 mutants and the FZD6 shRNA; Gene reporter activities are calculated as luciferase/renilla ratios, and are normalized to WT. **b** Quantitative RT-PCR analysis showing expression levels of FZD6, GNAS (gene encoding Gαs) and the PCP pathway downstream gene RHOA in SRA 01/04 cells transfected with WT FZD6, the indicated FZD6 mutants and the FZD6 shRNA; Data are mean ± s.e.m. ($n = 3$). Significance was determined by two-way ANOVA with Two-stage Benjamini, Krieger, & Yekutieli FDR procedure (****$P < 0.0001$, ***$P < 0.001$, **$P < 0.01$, *$P < 0.05$, n.s. not significant). **c** Western blotting assay showing protein expression levels of total-JNK (t-JNK), phospho-JNK (p-JNK, including p46 isoform and p54 isoform), RHOA, FZD6 and Gαs in SRA 01/04 cells transfected with WT FZD6, the indicated FZD6 mutants, negative control and the FZD6 shRNA. GAPDH or β-Actin was used as the loading control. **d** Scheme of primary culture of human lens epithelial explant. The anterior capsule with attached epithelium was peeled off in lens surgery and cultured with the epithelium side up. **e** Immunofluorescent staining of F-actin (red) and DAPI (blue) showed the primary cultured cells of the human lens epithelial explants treated with 200 ng/mL FGF-2 to induce fiber differentiation and then transfected with WT FZD6 or the indicated FZD6 mutant. White dashed line shows the capsule rim. White arrow showed the direction of cell polarity. Left panel scale bar: 200 μm; right panel scale bar: 20 μm. Data are representative images of three independent experiments.

determined six structures of three FZDs in both active and inactive states. ICL3 fusion strategy is commonly used for GPCR structural determination by crystallography[55] and cryo-EM approaches[56]. Fusion protein strategies for cryo-EM study was developed for GPCRs without the need of signaling proteins and can be used to solve antagonist bound or ligand-free (apo) receptor structures[56]. In the absence of agonist and signaling proteins, these receptors are trapped in an inactive conformation owing to the rigid attachment of BRIL to TM5 and TM6[29]. Together with inactive-to-active conformational comparison on each receptor, sequence conservation analysis and functional assessment, these structures reveal three FZD family-conserved molecular features ($W^{7.55}/R^{6.32}$ molecular switch, $P^{6.43}$ kink and the $W^{3.43}$–$Y^{6.40}$ interaction) that may constitute the structural basis of the activation mechanism of FZDs distinct from SMO and other GPCR classes. The bound G protein subtypes for different FZDs may vary, which could be related to their different physiological functions. In our comprehensive BRET study, we demonstrated that FZD1 primarily mediates constitutive Gq signaling while FZD3 and FZD6 are associated with Gs signaling. It is worth noting that apo FZD6 also exhibits considerable activity in G12 signaling and FZD1 may have constitutive activity in G11 signaling. Our structural analysis revealed that the diverse receptor-G protein interface sequences and interactions likely play a role in determining the specificity of FZD-G protein coupling. These observations systematically illustrate the general activation mechanism of the Class Frizzled receptors in the G protein signaling pathway, which provide some novel insight for understanding the Wnt/FZD signaling regulation and to guide drug discovery efforts targeting FZDs.

Among the ten FZDs, FZD6 and FZD3 are known to primarily mediate the non-canonical PCP signaling pathways. In particular, FZD6 can express broadly and function on epidermal derivatives and other tissue systems suitable for investigation of cell polarity and migration in the human lens models. In this study, based on the structural observation, we first performed mutagenesis and cell-based functional assay to uncover the key residues that would govern the G protein coupling to FZD6. We then conducted systematic cell imaging and functional analysis to investigate the role of these residues on the downstream PCP pathways in the human lens epithelial cell lines and primary culture of lens epithelial explant. Intriguingly, these mutations impaired PCP signaling by affecting the downstream protein expression, and further leading to the disordered cell migration and fiber alignment. Our findings suggested that the PCP signaling pathway may rely on the activation of FZD6 by coupling to the heterotrimeric G proteins, indicating that the FZD6-G protein interface may play an important role in the alignment and polarity of lens fibers thus provide a novel hotspot for therapeutic intervention for cataract pathogenesis.

Materials and methods
Cloning and expression of Frizzled receptors

The codon-optimized nucleotide sequence of human Frizzled-1 (FZD1; Uniprot ID: Q9UP38), Frizzled-3 (FZD3; Uniprot ID: Q9NPG1) and Frizzled-6 (FZD6; Uniprot ID: O60353) were synthesized by GenScript. For FZD1, the first 69 residues of FZD1 were removed. Haemagglutinin (HA) signal peptide, Flag tag, 10× His-tag and thermostabilized Escherichia coli apocytochrome b562RIL (BRIL) were added on the N terminus to enhance receptor expression and were then removed during purification with a tobacco etch virus (TEV) site. For FZD3, the first 22 residues and the last 124 residues of FZD3 and were removed. HA signal peptide, Flag tag, 10× His-tag and BRIL were added on the N terminus. For FZD6, the first 18 residues and the last 181 residues of FZD3 and were removed. HA signal peptide, Flag tag, BRIL and 10× His-tag were added on the N terminus. These three constructs were used to assemble the GPCR-G protein complex in vitro.

For the constructs of inactive FZD1, FZD3 and FZD6, additional modifications based on the above constructs for GPCR-G protein complex were introduced. Wild-type FZD1 (residues 70–515 and 528–637) was connected to BRIL using two short linkers derived from A_{2A} adenosine receptor (ARRQL between residue 515 and N-terminus of BRIL, and ARSTL between C-terminus of BRIL and residue 528); Wild-type FZD3 (residues 23–399 and 412–514) was connected to BRIL using two short linkers derived from A_{2A} adenosine receptor (ARRQL between residue 399 and N-terminus of BRIL, and ARSTL between C-terminus of BRIL and residue 412); Wild-type FZD6 (residues 19–395 and 408–510) was connected to BRIL using two short linkers derived from A_{2A} adenosine receptor (ARRQL between residue 395 and N-terminus of BRIL, and ARSTL between C-terminus of BRIL and residue 408).

Human FZD1, FZD3 and FZD6 were expressed in *Spodoptera frugiperda* Sf9 insect cells (Thermo Fisher) using the baculovirus method (Expression Systems), respectively. Cells were grown to a density of 2×10^6 cells per mL and then infected with bocavirus (MOI = 5). Cells were grown at 27 °C, collected by centrifugation 48 h after infection and cell pellets were stored at −80 °C for future use.

Purification of Frizzled receptors

The cell pellets of FZD1, FZD3 and FZD6 protein were thawed and washed with a low-salt buffer (10 mM HEPES pH 7.5, 20 mM KCl, 10 mM $MgCl_2$, protease inhibitor cocktail (Thermo Fisher)), and the supernatant was discarded by centrifugation at 35,000× *g* for 30 min. The cell pellets were followed by two washes with a high-salt buffer (10 mM HEPES pH 7.5, 1 M NaCl, 20 mM KCl, 10 mM $MgCl_2$ and protease inhibitor cocktail). Before solubilization, purified cell pellets were resuspended and incubated with 2 mg/mL iodoacetamide (Sigma) at 4 °C for 30 min. FZD protein was extracted from the membrane by adding HEPES, NaCl, n-dodecyl-β-D-maltoside (DDM) (Anatrace), and cholesteryl hemisuccinate (CHS, Sigma) to the membrane solution to a final concentration of 50 mM, 500 mM, 1.0% (w/v) and 0.2% (w/v), respectively, and stirred for 2 h at 4 °C. The supernatant was collected by centrifugation at 35,000× *g* for 30 min and incubated with TALON IMAC resin (Clontech) and 20 mM imidazole at 4 °C overnight.

For FZD1, the resin was centrifuged at 700× *g* for 15 min and washed with 15 column volumes of buffer I (50 mM HEPES pH 7.5, 500 mM NaCl, 5% (v/v) glycerol, 0.05% (w/v) DDM, 0.01% (w/v) CHS, 10 mM $MgCl_2$ and 20 mM imidazole) and followed by 8 column volumes of wash buffer II (25 mM HEPES pH 7.5, 100 mM NaCl, 5% (v/v) glycerol, 0.03% (w/v) DDM, 0.006% (w/v) CHS and 40 mM imidazole). After the resin was washed with 8

column volumes of buffer II, the wash buffer was changed to 3 column volumes of exchange buffer (50 mM HEPES pH 7.5, 500 mM NaCl, 10% (v/v) glycerol, 0.5% (w/v) lauryl maltose neopentyl glycol (LMNG) (Anatrace), 0.1% (w/v) CHS, 10 mM $MgCl_2$ and 20 mM imidazole) and incubated for 2 h at 4 °C. Then the resin was resuspended with 3 column volumes of buffer III (25 mM HEPES pH 7.5, 100 mM NaCl, 5% (v/v) glycerol, 0.03% (w/v) LMNG, 0.006% (w/v) CHS and 40 mM imidazole). TEV protease was added with a molar ratio of 1:20, and the mixture was incubated at 4 °C overnight. Next, the flow-through was collected and 3 column volumes of buffer III were added and collected. Finally, the protein solution was concentrated to ~2 mg/mL for future use.

For FZD3 and FZD6, the resin was centrifuged at 700× *g* for 15 min and washed with 5 column volumes of exchange buffer (50 mM HEPES pH 7.5, 500 mM NaCl, 10% (v/v) glycerol, 0.5% (w/v) LMNG, 0.08% (w/v) CHS, 0.02% (w/v) digitonin (Biosynth), 10 mM $MgCl_2$ and 20 mM imidazole) and incubated with 3 column volumes exchange buffer for 3 h at 4 °C. followed by 8 column volumes of wash buffer (25 mM HEPES pH 7.5, 100 mM NaCl, 10% (v/v) glycerol, 0.15% (w/v) LMNG, 0.024% (w/v) CHS, 0.006% (w/v) digitonin and 40 mM imidazole). Then the resin was eluted with 4 column volumes of elute buffer (25 mM HEPES pH 7.5, 100 mM NaCl, 10% (v/v) glycerol, 0.01% (w/v) LMNG, 0.0016% (w/v) CHS, 0.0004% (w/v) digitonin and 250 mM imidazole). Finally, the protein solution was concentrated to ~2 mg/mL for future use.

Cloning, expression and purification of miniGαs, miniGαq, Nb35 and VHH

miniGαs used in this paper was the same as that used in the structures of the A2AR–miniGs–Nb35[57] and GPR52-miniGs-Nb35[58]. MiniGαq was designed into a multifunctional chimera based on miniGαs (same method as miniGs/15, miniG15[59]). In brief, the specificity determinants (α5) of Gαq were transferred onto miniGαs, providing possible binding sites for Nb35 antibody to stabilize the G protein heterotrimer. The Nb35 was cloned in pET22b vector with a C-terminal 6× His tag. The anti-Fab Nb (VHH) was cloned in pET26b(+) vector with an N-terminal 6× His tag. MiniGαs, miniGαq, Nb35 and VHH were expressed in *E. coli* strain BL21 (DE3) cells and purified by Ni-NTA chromatography (GenScript).

For the purification of miniGα protein[60], the pellets from 1 L of *E. coli* culture (miniGαs or miniGαq) were resuspended in buffer (40 mM HEPES pH 7.5, 100 mM NaCl, 10% glycerol, 10 mM imidazole, 5 mM $MgCl_2$, 100 μM GDP, 100 μg/mL lysozyme, 50 μg/mL DNase I, 100 μM DTT and protease inhibitor cocktail) and lysed by sonication. The supernatant was discarded by centrifugation at 35,000× *g* for 30 min and loaded onto 2 mL Ni^{2+} affinity chromatography. The column was washed

with 30 mL of buffer (20 mM HEPES pH 7.5, 500 mM NaCl, 10% glycerol, 40 mM imidazole, 1 mM $MgCl_2$, 50 μM GDP). The column was eluted with 6 mL buffer (20 mM HEPES pH 7.5, 100 mM NaCl, 10% glycerol, 400 mM imidazole, 1 mM $MgCl_2$, 50 μM GDP). The protein solution was concentrated to a volume of 2 mL and loaded onto a Superdex200 10/600 column (GE) in buffer (10 mM HEPES pH 7.5, 100 mM NaCl, 10% glycerol, 1 mM $MgCl_2$, 10 μM GDP and 1 mM TCEP). Peak fractions of miniGα protein were concentrated to 20 mg/mL for future use.

For the purification of Nb35 protein[60,61] and VHH[29] protein, the pellet was resuspended from 1 L of *E. coli* culture in buffer (20 mM HEPES pH 7.5, 100 mM NaCl, 10 mM imidazole, 5 mM $MgCl_2$, complete protease tablets, 50 μg/mL DNase I and 100 μg/mL lysozyme) and lysed by sonication. The supernatant was discarded by centrifugation at 35,000× g for 30 min and loaded onto 2 mL Ni^{2+} affinity chromatography. The column was washed with 20 mL of buffer (20 mM HEPES pH 7.5, 500 mM NaCl, 40 mM imidazole) and eluted with 6 mL buffer (20 mM HEPES pH 7.5, 100 mM NaCl, 500 mM imidazole). The protein solution was concentrated to a volume of 1 mL and loaded onto a Superdex200 10/300 column (GE) in buffer (10 mM HEPES pH 7.5, 100 mM NaCl, 10% glycerol). Peak fractions of Nb35 protein and VHH protein were concentrated to 20 mg/mL for future use, respectively.

Cloning, expression and purification of Gβ1γ2 and anti-BRIL Fab

Both the human heterodimeric Gβ1γ2 (Gγ2 contain a C68S mutation) and anti-Bril Fab were cloned into pFastbac-Dual vector with a C-terminal 6× His tag. The human heterodimeric Gβ1γ2 was expressed in *Spodoptera frugiperda* Sf9 insect cells and the anti-Bril Fab was expressed in secreted form from *Trichuplusia ni* Hi5 insect cells using the baculovirus method (Expression Systems), respectively. Cells were grown to a density of 2×10^6 cells per ml and then infected with bocavirus (MOI = 5). Cells were grown at 27 °C, and cell pellets and supernatant were collected by centrifugation 48 h after infection.

For the purification of heterodimeric Gβ1γ2 protein[61], the cell pellets from 2 L of Gβ1γ2 were thawed and resuspended to 50 mL in buffer (30 mM Tris pH 8.0, 100 mM NaCl, 5 mM $MgCl_2$, 5 mM imidazole, complete protease tablets, 50 μg/mL DNase I and 100 μM DTT). Cells were broken by sonication and clarified by centrifugation (38,000× g for 1 h). The supernatant was loaded onto 2 mL Ni^{2+} affinity chromatography. The column was washed with 20 mL of buffer (20 mM Tris pH 8.0, 300 mM NaCl, 30 mM imidazole, 10% glycerol and 1 mM $MgCl_2$), and eluted with 6 mL buffer (20 mM Tris pH 9.0,

50 mM NaCl, 500 mM imidazole, 10% glycerol and 1 mM $MgCl_2$). The elute was diluted to 60 mL in buffer (20 mM Tris pH 9.0, 50 mM NaCl, 10% glycerol, 1 mM $MgCl_2$, 1 mM DTT) and loaded onto a 5 mL Q FF column (GE Healthcare) at 5 mL/min. The Q FF column was washed with 40 mL buffer (20 mM Tris pH 9.0, 50 mM NaCl, 10% glycerol, 1 mM $MgCl_2$, 1 mM DTT) and eluted with a linear gradient of 50-300 mM NaCl in buffer (20 mM Tris pH 9.0, 50 mM NaCl, 10% glycerol, 1 mM $MgCl_2$, 1 mM DTT). The protein solution was concentrated to a volume of 1 mL and loaded onto a Superdex200 10/300 column (GE) in buffer (10 mM HEPES pH 7.5, 100 mM NaCl, 10% glycerol, 1 mM $MgCl_2$, 0.1 mM TCEP). Peak fractions of heterodimeric Gβ1γ2 protein were concentrated to 5 mg/mL for future use.

For the purification of anti-Bril Fab, the cell pellets from 1 L of anti-Bril Fab were centrifuged at 2000× g for 30 min, and the 1 L supernatant was loaded onto a 2 mL Ni-NTA resin. The column was washed with 15 CV of wash buffer (20 mM Tris-HCI pH 7.55, 150 mM NaCl, and 20 mM imidazole) and the protein was eluted with the same buffer supplemented with 250 mM imidazole, the protein was collected and purified over gel filtration chromatography using a Superdex 200 10/300 column (GE) equilibrated in the buffer (20 mM Tris-HCI pH 7.55, 100 mM NaCl, and 10% glycerol). Monomeric fractions were pooled, concentrated to 4 mg/mL with a 30-kDa cut-off concentrator (Millipore), and flash frozen in liquid nitrogen, then stored at −80 °C for further use.

Complex formation for cryo-EM sample preparation

About the complex formation of Frizzled-G protein. Purified Frizzled receptor, heterodimeric Gβ1γ2, miniGαs (or miniGαq), and Nb35 were mixed in a 1:1.2:1.5:2 molar ratio followed by the addition of apyrase (1 unit), respectively. The mixture was incubated at 4 °C overnight. The FZD1-Gq (FZD3-Gs or FZD6-Gs) complex was loaded on size-exclusion chromatography (Superdex 200 10/300 GL column, GE) in SEC buffer (20 mM HEPES pH 7.5, 100 mM NaCl, 0.00075% (w/v) LMNG, 0.00025% (w/v) glyco-diosgenin (GDN, Anatrace), 0.00025% (w/v) CHS, and 100 μM DTT). Peak fractions containing FZD-G protein complex were concentrated to 2.5 mg/mL for electron microscopy studies.

About the complex formation of inactive Frizzled protein. Purified Frizzled receptor, anti-BRIL Fab and VHH were mixed in a 1:1.5:2 molar ratio, respectively. The mixture was incubated at 4 °C overnight. The FZD1-Fab-VHH (FZD3-Fab-VHH or FZD6-Fab-VHH) complex was loaded on size-exclusion chromatography (Superdex 200 10/300 GL column, GE) in SEC buffer (20 mM HEPES pH 7.5, 100 mM NaCl, 0.00075% (w/v) LMNG, 0.00025% (w/v) GDN, 0.00025% (w/v) CHS, and 100 μM DTT). Peak fractions containing complex were

concentrated to 2.5 mg/mL for electron microscopy studies.

Cryo-EM sample preparation and data collection

3 μL of the purified samples (FZD-G protein complex or FZD-Fab-VHH complex) at a concentration of around 2.5 mg/mL were applied to glow-discharged 300-mesh Au grids (Quantifoil, R1.2/1.3). Excessive sample was removed by blotting with filter paper for 3.5 s before plunge-freezing in liquid ethane using a FEI Vitrobot Mark IV at 100% humidity and 8 °C.

Five datasets (FZD3-Gs, FZD6-Gs, FZD1-Fab-VHH, FZD3-Fab-VHH and FZD6-Fab-VHH) were collected on a Titan Krios 300 kV electron microscope (Thermo Fisher Scientifics, USA) equipped with a GIF Quantum energy filter (20 eV energy slit width, Gatan Inc., USA). These five datasets were recorded by a K3 camera (Gatan) at a nominal magnification of 105,000 (calibrated pixel size: 0.832 Å/pixel) and 15 e^-/pixel^2/s. The movies were recorded using the super resolution counting mode by SerialEM which applied the beam image shift acquisition method with one image near the edge of each hole. A 50 μm C2 aperture was always inserted during the data collection period. The defocus ranged from –0.7 to –2.2 μm. For each movie stack, a total of 40 frames were recorded, yielding a total dose of 60 e^-/Å^2. FZD1-Gq datasets were collected on a Titan Krios 300 kV electron microscope equipped without an energy filter. This dataset was recorded by a K3 camera (Gatan) at a nominal magnification of 29,000 (calibrated pixel size: 0.82 Å/pixel) and a defocus range of –0.7 to –2.2 μm. For each movie stack, a total of 40 frames were recorded, yielding a total dose of 60 e^-/Å^2.

Cryo-EM image processing

For FZD1-Gq complex and FZD1-Fab-VHH complex, 7,650 and 4,396 movies were recorded and processed with cryoSPARC[62]. Patch motion correction was used for beam-induced motion correction. Then, contrast transfer function (CTF) parameters for each dose-weighted micrograph were estimated by patch CTF estimation. Only images with the highest resolution of less than 4 Å were selected for further processing. A total of 6,650 and 4,242 images were selected for auto blob picking, and particles were extracted to do 2D classification. 2D class averages with diverse orientations and clear secondary features were selected as 2D templates for another round of autopicking process by cryoSPARC. A total of 935,627 and 628,701 particles were selected from good 2D classification to generate the initial models. These particles and initial models were used to do 3D classification in heterogeneous refinement in cryoSPARC. 544,329 and 327,768 particles were selected for the final homogeneous refinement followed by nonuniform refinement and local

refinement in cryoSPARC, resulting in density map with nominal resolution of 3.6 Å and 3.5 Å for the FZD1-Gq complex and FZD1-Fab-VHH complex (determined by gold-standard Fourier shell correlation (FSC), 0.143 criterion). Estimation of local resolution was performed in cryoSPARC. Both density maps were performed by automatic masking and local sharpening in DeepEMhancer[63] to optimize the local density.

For FZD3-Gs complex, 6,801 movies were recorded and processed with cryoSPARC. Patch motion correction was used for beam-induced motion correction. Then, contrast transfer function (CTF) parameters for each dose-weighted micrograph were estimated by patch CTF estimation. Only images with the highest resolution of less than 4 Å were selected for further processing. 6,254 images were selected for auto blob picking, and particles were extracted to do 2D classification. 2D class averages with diverse orientations and clear secondary features were selected as 2D templates for another round of autopicking process by cryoSPARC. 1,213,683 particles were selected from good 2D classification to generate the initial models. These particles and initial models were used to do 3D classification in heterogeneous refinement in cryoSPARC. 294,949 particles were selected for homogeneous refinement followed by nonuniform refinement and local refinement in cryoSPARC, resulting in density map with nominal resolution of 3.22 Å. The map and particles from local refinement were used to do 3D variability and 3D classification and output 3 components and 30 classes. We used particles from local refinement and selected 3 better volumes from 3D variability and 3D classification to do two heterogeneous refinements separately. Then the particles from the best class of each heterogeneous refinement were merged by removing duplicates particles. And several rounds of heterogeneous refinements were done using the merged particles and volumes chosen above. The best particles and model selected from the last round heterogeneous refinement were used to do further refinement. At last, 89,795 particles were selected for the final homogeneous refinement followed by nonuniform refinement and local refinement, resulting in density map with nominal resolution of 3.50 Å (determined by gold-standard Fourier shell correlation (FSC), 0.143 criterion). Estimation of local resolution was performed in cryoSPARC. The density map from the final local refinement was sharpened by a global B-factor.

For FZD6-Gs complex, 11,207 movies were recorded and processed with cryoSPARC. Patch motion correction was used for beam-induced motion correction. Then, contrast transfer function (CTF) parameters for each dose-weighted micrograph were estimated by patch CTF

estimation. Only images with the highest resolution of less than 4 Å were selected for further processing. 9565 images were selected for auto blob picking, and particles were extracted to do 2D classification. 2D class averages with diverse orientations and clear secondary features were selected as 2D templates for another round of autopicking process by cryoSPARC. 1,041,782 particles were selected from good 2D classification to generate the initial models. These particles and initial models were used to do 3D classification in heterogeneous refinement in cryoSPARC. 530,390 particles were selected for homogeneous refinement followed by nonuniform refinement and local refinement with a mask in TM region in cryoSPARC, resulting in a density map of TM region with nominal resolution of 3.40 Å. The TM region map was use for further heterogeneous refinement. The best class with 299,023 particles was used for nonuniform refinement and local refinement after a per-perticle local CTF refinement, resulting in density map with nominal resolution of 3.40 Å (determined by gold-standard Fourier shell correlation (FSC), 0.143 criterion). Estimation of local resolution was performed in cryoSPARC. Density maps were performed by automatic masking and local sharpening in DeepEMhancer to optimize the local density.

For FZD3-Fab-VHH complex and FZD6-Fab-VHH complex, 6,443 and 4,946 movies were recorded and processed with cryoSPARC. Patch motion correction was used for beam-induced motion correction. Then, contrast transfer function (CTF) parameters for each dose-weighted micrograph were estimated by patch CTF estimation. Only images with the highest resolution of less than 4 Å were selected for further processing. A total of 5,915 and 4,865 images were selected for auto blob picking, and particles were extracted to do 2D classification. Particles in 2D class averages with diverse orientations and clear secondary features were selected to train a model and perform particle picking using Topaz[64] by cryoSPARC. A total of 620,258 and 1,156,464 particles were selected from good 2D classification to generate the initial models. These particles and initial models were used to do 3D classification in heterogeneous refinement in cryoSPARC. 221,700 and 660,274 particles were selected for the final homogeneous refinement followed by nonuniform refinement and local refinement in cryoSPARC, resulting in density map with nominal resolution of 3.38 Å and 3.30 Å for the FZD3-Fab-VHH complex and FZD6-Fab-VHH complex, respectively (determined by gold-standard Fourier shell correlation (FSC), 0.143 criterion). Estimation of local resolution was performed in cryoSPARC. Density maps were performed by automatic masking and local sharpening in DeepEMhancer to optimize the local density.

Cryo-EM model building and refinement

The homology models of FZD1, FZD3 and FZD6 were initially generated by Alphafold[65]. For Gs trimer and Nb35, the model 6LI3[58] (PDB) was chosen. For BRIL, anti-BRIL Fab and VHH, the model 6WW2[29] (PDB) was chosen. Each part of the target models was docked into the electron microscopy density map using UCSF Chimera[66]. Then, these models were used for model building and refinement against the electron density map. Subsequently, the generated model was manually adjusted in Coot[67] followed by automatic real space refinement in real space in Phenix[68] for several iterations. The model statistics were validated using Phenix v1.20. The final refinement statistics from the comprehensive validation of Phenix v1.20. are provided in Supplementary Table S1.

BRET2 TRUPATH assay

To measure the dissociation of Gαβγ heterotrimer directly, we applied the BRET2 assay system as reported before[22]. In brief, HEK293T cells were plated in a 6-well plate. After 2 h, cells were transiently co-transfected with plasmids encoding WT or mutated FZD together with G protein BRET probe (Gαs-RLuc8 (or Gαq-RLuc8), Gβ3, Gγ9-GFP2) using Lipofectamine 2000 reagent (Thermo Fisher). The plasmids of Gαq-RLuc8, Gβ3, Gγ9-GFP2, and FZD1 were co-transfected at a plasmid ratio of 1:1:1:2.5. The plasmids of Gαs-Rluc8, Gβ3, Gγ9-GFP2, and FZD3 (or FZD6) were co-transfected at a plasmid ratio of 1:1:1:2. 24 h after transfection, cells were distributed into a 96-well microplate (30,000–50,000 cells per well) and incubated for additional 24 h at 37 °C. For the constitutive activity measurement, white backings (Perkin Elmer) were applied to the plate bottoms. The transfected cells were washed once with HBSS and supplemented with 100 μL of 5 μM coelenterazine 400a (Nanolight Technologies). Plates were read in EnVision plate reader (Perkin Elmer) with 410 nm (RLuc8-coelenterazine 400a) and 515 nm (GFP2) emission filters with an integration time of 1 s per well. The GFP2 emission to RLuc8 emission ratio was used to compute the BRET2 ratios. Cell-surface expression for each mutant was monitored by a fluorescence-activated cell sorting (FACS) assay. In brief, the expressed cells were incubated with mouse anti-Flag (M2–fluorescein isothiocyanate (FITC)) antibody (Sigma) for 20 min at 4 °C, and then a ninefold excess of PBS was added to cells. Finally, the surface expression of FZD receptor was monitored by detecting the fluorescent intensity of FITC using a Guava EasyCyte HT system (Millipore)[58]. Statistics are provided in Supplementary Table S2.

Transfection in SRA01/04 cell line

Lens epithelial cells were previously reported to have relatively strong constitutive expression of FZD6 and

activation of WNT signaling pathways[11,69]. We adopted human lens epithelial cell line SRA 01/04 in the functional assays of downstream pathways. Cells were cultured in the Dulbecco's Modified Eagle Medium (DMEM, Sigma-Aldrich) supplemented with 10% fetal bovine serum (FBS, #10099141, Gibco) seeded in six-well plate (for quantitative RT-PCR and western blot) or 24-well plate (for Luciferase assay) overnight and were then transfected with wild type (WT) FZD6, the indicated FZD6 mutant plasmids and FZD6 shRNA. The sequence of FZD6 shRNA was: top 5′-TTTGAATTGTGCTTCAG-GAAGAACTCACTTCCTGTCATGAGTTCTTCCTGA AGCACAATTATTTTT - 3′; bottom 5′- CTAGAAAA ATAATTGTGCTTCAGGAAGAACTCATGACAGGA AGTGAGTTCTTCCTGAAGCACAATTC-3′.

Luciferase assay

An ATF2-Luc reporter plasmid[70] and TOPFlash plasmid (Beyotime) were employed to detect the activity of PCP pathway and β-catenin pathway, respectively. Cells were transfected and 300 ng of WT FZD6, mutant plasmids, or FZD6 shRNA, and then co-transfected with 300 ng of ATF2/TOP luciferase reporters and 20 ng pRL-tk. Transfections were normally carried out in triplicate wells. 48 h after transfection of reporters, cells were washed twice with PBS and lysed in Passive Lysis Buffer (Promega). Luciferase activity was measured using the Dual Glo Luciferase Assay System (Promega) as instructed by the manufacturers. Gene reporter activities were calculated as luciferase/renilla ratios. Statistics are provided in Supplementary Table S3.

Quantitative RT-PCR

After 48 h of transfection, cells were collected and total RNA was extracted using TRIzol reagent (Thermo Fisher), cDNA was generated using HiFiScript gDNA removal cDNA Synthesis Kit (ComWin Biotech) following the manufacturers' instructions. Gene expression was quantified by real-time PCR with GAPDH used as an endogenous control gene. The primers used were listed here.

h-GAPDH-FATTGCCCTCAACGACCACT
h-GAPDH-RATGAGGTCCACCACCCTGT
h-FZD6-FGGCTTGTATCTTGTGCCATTAG
h-FZD6-RGGGATATGGTACTGACGACAAT
h-GNAS-FTGCCTCGGGAACAGTAAGAC
h-GNAS-RGCCGCCCTCTCCATTAAAC
h-RHOA-FAGGAAGATTATGATCGCCTGAG
h-RHOA-RCTAAACTATCAGGGCTGTCGAT

Western blot analysis

After 48 h of transfection, SRA01/04 cell lysates were obtained using RIPA lysis buffer (Beyotime) supplemented immediately before use with 10 μL/mL phosphatase and protease inhibitors (PhosSTOPTM, Roche). The bicinchoninic acid assay (Beyotime) was used to measure total protein content to enable equal loading of protein onto 4%–12% precast mini polyacrylamide gels (SurePAGE™, GenScript). Proteins were transferred onto polyvinyl difluoride (PVDF) membranes, which were then blocked with TBST containing 0.5% w/v skim milk, hybridized with primary antibody against total-JNK (sc-7345, Santa), phosphor-JNK (sc-293136, Santa), RHOA (sc-418, Santa), FZD6 (ab290728, Abcam, UK), GNAS (10150-2-ap, Proteintech) or β-Actin (66099-1-lg, Proteintech) or GAPDH (ab8245, Abcam) overnight, followed by incubation with secondary antibody conjugated with horseradish peroxidase (GE). Proteins were then detected using ECL chemiluminescent substrate (BL520A, biosharp) and visualized with a chemiluminescence gel imaging system (Peiqing).

Lens epithelial explant collection, cell culture and treatment

All human samples were gathered from patients having lens replacement surgery at Eye & ENT Hospital of Fudan University (Shanghai, China) in accordance with the Declaration of Helsinki. By the standard step of capsulorhexis during lens surgery, the anterior capsule with attached epithelium was peeled off and collected (lens epithelium would otherwise be discarded if not for research purpose)[71,72]. Lens epithelial explants were primarily cultured with the epithelium side up in the DMEM supplemented with 20% FBS (Gibco) in 37 °C and 5% CO_2, with medium changed every other day. For the fibroblast growth factor 2 (FGF-2) induced lens differentiation model, explants were treated with 200 ng/mL human FGF-2 (233-10; R&D) for 48–72 h. Explants were then transfected with WT FZD6 or the mutant plasmid.

This study was reviewed and approved by the Ethics Committee of the Eye & Ear, Nose, and Throat (ENT) Hospital of Fudan University, Shanghai, China in accordance with applicable regulations (No. 2014055). Written informed consents were obtained before surgery from each patient for the use of their lens tissues (would otherwise be discarded if not for research purpose). All procedures adhered to the tenets of Declaration of Helsinki.

Immunofluorescence staining analysis

The Lens epithelial explants were fixed with 4% paraformaldehyde for 30 min, blocked in PBS solution containing 0.3% Triton X-100 and 3% BSA for 30 min, followed by incubation with TRITC Phalloidin (40734ES75, Yeasen, 1:200 for F-actin staining) and DAPI (40728ES03, Yeasen, 1:1000 for nuclei staining) at room temperature away from light for 1 h. After washed with PBS for three times, images were obtained using a Leica DM3000 microscope system.

Author details

[1]iHuman Institute, ShanghaiTech University, Shanghai, China. [2]School of Life Science and Technology, ShanghaiTech University, Shanghai, China. [3]Eye Institute and Department of Ophthalmology, Eye & ENT Hospital, Fudan University, Shanghai, China. [4]Shanghai Clinical Research and Trial Center, Shanghai, China

Author contributions

Z.Z. performed protein purification, data collection and structure determination of FZD3 and FZD6 complexes; X.L. performed protein purification, data collection, structure determination of FZD1 complexes and assisted construct design of FZD3/6$_{ICL3}$BRIL; Z.Z. and X.L. performed structure analysis and BRET assays; L.Wei performed luciferase assays, quantitative RT-PCR assay, Western blot and immunostaining analysis; Y.W. performed structural analysis; L.X. optimized the protein expression of FZD6 at early phase of the project; L.Wu assisted cryo-EM data processing; X.W. cultured HEK293T cells for functional assays; X.Z. supervised the PCP signaling assays; F.X. designed, coordinated and supervised all experiments; Z.Z., X.L., L.Wei and F.X. wrote the manuscript. All authors contributed to data interpretation and preparation of the manuscript.

Data availability

The cryo-EM density maps have been deposited in the Electron Microscopy Data Bank (EMDB) under accession codes EMD-36111 (FZD1–Gs complex), EMD-36112 (FZD1 in apo inactive state), EMD-36266 (FZD3–Gs complex), EMD-36262 (FZD3 in apo inactive state), EMD-36261 (FZD6–Gs complex) and EMD-36258 (FZD6 in apo inactive state). Coordinates have been deposited in the Protein Data Bank (PDB) under accession codes 8J9N (FZD1–Gs complex), 8J9O (FZD1 in apo inactive state), 8JHI (FZD3–Gs complex), 8JHC (FZD3 in apo inactive state), 8JHB (FZD6–Gs complex) and 8JH7 (FZD6 in apo inactive state).

Conflict of interest

The authors declare no competing interests.

Publisher's note

Springer Nature remains neutral with regard to jurisdictional claims in published maps and institutional affiliations.

Supplementary information The online version contains supplementary material available at https://doi.org/10.1038/s41421-023-00627-y.

References

1. Schulte, G. & Wright, S. C. Frizzleds as GPCRs—More conventional than we thought! *Trends Pharm. Sci.* **39**, 828–842 (2018).
2. Dijksterhuis, J. P., Petersen, J. & Schulte, G. WNT/Frizzled signalling: receptor-ligand selectivity with focus on FZD-G protein signalling and its physiological relevance: IUPHAR Review 3. *Br. J. Pharm.* **171**, 1195–1209 (2014).
3. Wang, Y., Chang, H., Rattner, A. & Nathans, J. Frizzled receptors in development and disease. *Curr. Top. Dev. Biol.* **117**, 113–139 (2016).
4. Yang, S. et al. Crystal structure of the Frizzled 4 receptor in a ligand-free state. *Nature* **560**, 666–670 (2018).
5. Katoh, M. WNT/PCP signaling pathway and human cancer (Review). *Oncol. Rep.* **14**, 1583–1588 (2005).
6. Kohn, A. D. & Moon, R. T. Wnt and calcium signaling: β-Catenin-independent pathways. *Cell Calcium* **38**, 439–446 (2005).
7. Bornens, M. Organelle positioning and cell polarity. *Nat. Rev. Mol. Cell Biol.* **9**, 874–886 (2008).
8. Jan, Y.-N. & Jan, L. Y. Polarity in cell division: What frames thy fearful asymmetry? *Cell* **100**, 599–602 (2000).
9. Koca, Y., Collu, G. M. & Mlodzik, M. Wnt-frizzled planar cell polarity signaling in the regulation of cell motility. *Curr. Top. Dev. Biol.* **150**, 255–297 (2022).
10. Gray, R. S., Roszko, I. & Solnica-Krezel, L. Planar cell polarity: Coordinating morphogenetic cell behaviors with embryonic polarity. *Dev. Cell* **21**, 120–133 (2011).
11. Dawes, L. J., Sugiyama, Y., Tanedo, A. S., Lovicu, F. J. & McAvoy, J. W. Wnt-frizzled signaling is part of an FGF-induced cascade that promotes lens fiber differentiation. *Investig. Ophthalmol. Vis. Sci.* **54**, 1582–1590 (2013).
12. Sugiyama, Y. et al. Secreted frizzled-related protein disrupts PCP in eye lens fiber cells that have polarised primary cilia. *Dev. Biol.* **338**, 193–201 (2010).
13. Sugiyama, Y., Akimoto, K., Robinson, M. L., Ohno, S. & Quinlan, R. A. A cell polarity protein aPKCλ is required for eye lens formation and growth. *Dev. Biol.* **336**, 246–256 (2009).
14. Corda, G. & Sala, A. Non-canonical WNT/PCP signalling in cancer: Fzd6 takes centre stage. *Oncogenesis* **6**, e364 (2017).
15. Hansen, C. et al. Wnt-5a-induced phosphorylation of DARPP-32 inhibits breast cancer cell migration in a CREB-dependent manner. *J. Biol. Chem.* **284**, 27533–27543 (2009).
16. Cantilena, S. et al. Frizzled receptor 6 marks rare, highly tumourigenic stem-like cells in mouse and human neuroblastomas. *Oncotarget* **2**, 976–983 (2011).
17. Planutis, K., Planutiene, M., Nguyen, A. V., Moyer, M. P. & Holcombe, R. F. Invasive colon cancer, but not non-invasive adenomas induce a gradient effect of Wnt pathway receptor frizzled 1 (Fz1) expression in the tumor microenvironment. *J. Transl. Med.* **11**, 50 (2013).
18. Xu, L. et al. Cryo-EM structure of constitutively active human Frizzled 7 in complex with heterotrimeric G(s). *Cell Res.* **31**, 1311–1314 (2021).
19. Nichols, A. S., Floyd, D. H., Bruinsma, S. P., Narzinski, K. & Baranski, T. J. Frizzled receptors signal through G proteins. *Cell. Signal.* **25**, 1468–1475 (2013).
20. Schulte, G. International union of basic and clinical pharmacology. LXXX. The class Frizzled receptors. *Pharm. Rev.* **62**, 632–667 (2010).
21. Wright, S. C. et al. A conserved molecular switch in Class F receptors regulates receptor activation and pathway selection. *Nat. Commun.* **10**, 667 (2019).
22. Olsen, R. H. J. et al. TRUPATH, an open-source biosensor platform for interrogating the GPCR transducerome. *Nat. Chem. Biol.* **16**, 841–849 (2020).
23. Olsen, R. H. J. & English, J. G. Advancements in G protein-coupled receptor biosensors to study GPCR-G protein coupling. *Br. J. Pharmacol.* **180**, 1433–1443 (2023).
24. Nehmé, R. et al. Mini-G proteins: Novel tools for studying GPCRs in their active conformation. *PLoS One* **12**, e0175642 (2017).
25. Qi, X. et al. Cryo-EM structure of oxysterol-bound human Smoothened coupled to a heterotrimeric G(i). *Nature* **571**, 279–283 (2019).
26. Wang, C. et al. Structure of the human smoothened receptor bound to an antitumour agent. *Nature* **497**, 338–343 (2013).
27. Chun, E. et al. Fusion partner toolchest for the stabilization and crystallization of G protein-coupled receptors. *Structure* **20**, 967–976 (2012).
28. Robertson, M. J. et al. Structure determination of inactive-state GPCRs with a universal nanobody. *Nat. Struct. Mol. Biol.* **29**, 1188–1195 (2022).
29. Tsutsumi, N. et al. Structure of human Frizzled5 by fiducial-assisted cryo-EM supports a heterodimeric mechanism of canonical Wnt signaling. *eLife* **9**, e58464 (2020).
30. Zhang, Y. et al. Single-particle cryo-EM structural studies of the β(2)AR-Gs complex bound with a full agonist formoterol. *Cell Discov.* **6**, 45 (2020).
31. Liu, X. et al. Mechanism of intracellular allosteric β2AR antagonist revealed by X-ray crystal structure. *Nature* **548**, 480–484 (2017).
32. Song, G. et al. Human GLP-1 receptor transmembrane domain structure in complex with allosteric modulators. *Nature* **546**, 312–315 (2017).
33. Zhang, Y. et al. Cryo-EM structure of the activated GLP-1 receptor in complex with a G protein. *Nature* **546**, 248–253 (2017).
34. Lin, S. et al. Structures of Gi-bound metabotropic glutamate receptors mGlu2 and mGlu4. *Nature* **594**, 583–588 (2021).
35. Dijkgraaf, G. J. P. et al. Small molecule inhibition of GDC-0449 refractory smoothened mutants and downstream mechanisms of drug resistance. *Cancer Res.* **71**, 435–444 (2011).

36. Qi, X., Friedberg, L., De Bose-Boyd, R., Long, T. & Li, X. Sterols in an intramolecular channel of Smoothened mediate Hedgehog signaling. *Nat. Chem. Biol.* **16**, 1368–1375 (2020).

37. Rasmussen, S. G. et al. Crystal structure of the β2 adrenergic receptor-Gs protein complex. *Nature* **477**, 549–555 (2011).

38. Carpenter, B., Nehmé, R., Warne, T., Leslie, A. G. & Tate, C. G. Structure of the adenosine A(2A) receptor bound to an engineered G protein. *Nature* **536**, 104–107 (2016).

39. Xu, P. et al. Structural insights into the lipid and ligand regulation of serotonin receptors. *Nature* **592**, 469–473 (2021).

40. Hua, T. et al. Activation and signaling mechanism revealed by cannabinoid receptor-G(i) complex structures. *Cell* **180**, 655–665.e18 (2020).

41. Liu, S. et al. Differential activation mechanisms of lipid GPCRs by lysophosphatidic acid and sphingosine 1-phosphate. *Nat. Commun.* **13**, 731 (2022).

42. Chen, H. et al. Structure of S1PR2-heterotrimeric G(13) signaling complex. *Sci. Adv.* **8**, eabn0067 (2022).

43. Zhao, C. et al. Structural insights into sphingosine-1-phosphate recognition and ligand selectivity of S1PR3-Gi signaling complexes. *Cell Res* **32**, 218–221 (2022).

44. Yuan, Y. et al. Structures of signaling complexes of lipid receptors S1PR1 and S1PR5 reveal mechanisms of activation and drug recognition. *Cell Res.* **31**, 1263–1274 (2021).

45. Liang, Y. L. et al. Phase-plate cryo-EM structure of a biased agonist-bound human GLP-1 receptor-Gs complex. *Nature* **555**, 121–125 (2018).

46. Liang, Y. L. et al. Cryo-EM structure of the active, G(s)-protein complexed, human CGRP receptor. *Nature* **561**, 492–497 (2018).

47. Liang, Y. L. et al. Phase-plate cryo-EM structure of a class B GPCR-G-protein complex. *Nature* **546**, 118–123 (2017).

48. Ping, Y. Q. et al. Structures of the glucocorticoid-bound adhesion receptor GPR97-G(o) complex. *Nature* **589**, 620–626 (2021).

49. Flock, T. et al. Universal allosteric mechanism for Gα activation by GPCRs. *Nature* **524**, 173–179 (2015).

50. Putnova, I. et al. Angled growth of the dental lamina is accompanied by asymmetrical expression of the WNT pathway receptor frizzled 6. *Front. Physiol.* **8**, 29 (2017).

51. Takagishi, M., Esaki, N., Takahashi, K. & Takahashi, M. Cytoplasmic dynein functions in planar polarization of basal bodies within ciliated cells. *iScience* **23**, 101213 (2020).

52. Tian, T. et al. Somatic mutations in planar cell polarity genes in neural tissue from human fetuses with neural tube defects. *Hum. Genet.* **139**, 1299–1314 (2020).

53. Liu, H., Mohamed, O., Dufort, D. & Wallace, V. A. Characterization of Wnt signaling components and activation of the Wnt canonical pathway in the murine retina. *Dev. Dyn.* **227**, 323–334 (2003).

54. Chen, Y., Stump, R. J. W., Lovicu, F. J., Shimono, A. & McAvoy, J. W. Wnt signaling is required for organization of the lens fiber cell cytoskeleton and development of lens three-dimensional architecture. *Dev. Biol.* **324**, 161–176 (2008).

55. Thompson, A. A. et al. Structure of the nociceptin/orphanin FQ receptor in complex with a peptide mimetic. *Nature* **485**, 395–399 (2012).

56. Zhang, K., Wu, H., Hoppe, N., Manglik, A. & Cheng, Y. Fusion protein strategies for cryo-EM study of G protein-coupled receptors. *Nat. Commun.* **13**, 4366 (2022).

57. García-Nafría, J., Lee, Y., Bai, X., Carpenter, B. & Tate, C. G. Cryo-EM structure of the adenosine A(2A) receptor coupled to an engineered heterotrimeric G protein. *Elife* **7**, e35946 (2018).

58. Lin, X. et al. Structural basis of ligand recognition and self-activation of orphan GPR52. *Nature* **579**, 152–157 (2020).

59. Lin, X. et al. Cryo-EM structures of orphan GPR21 signaling complexes. *Nat. Commun.* **14**, 216 (2023).

60. Carpenter, B. & Tate, C. G. Expression and purification of Mini G proteins from Escherichia coli. *Bio Protoc.* **7**, e2235 (2017).

61. Carpenter, B. & Tate, C. G. Engineering a minimal G protein to facilitate crystallisation of G protein-coupled receptors in their active conformation. *Protein Eng. Des. Sel.* **29**, 583–594 (2016).

62. Punjani, A., Rubinstein, J. L., Fleet, D. J. & Brubaker, M. A. cryoSPARC: algorithms for rapid unsupervised cryo-EM structure determination. *Nat. Methods* **14**, 290–296 (2017).

63. Sanchez-Garcia, R. et al. DeepEMhancer: a deep learning solution for cryo-EM volume post-processing. *Commun. Biol.* **4**, 874 (2021).

64. Bepler, T. et al. Positive-unlabeled convolutional neural networks for particle picking in cryo-electron micrographs. *Nat. Methods* **16**, 1153–1160 (2019).

65. Jumper, J. et al. Highly accurate protein structure prediction with AlphaFold. *Nature* **596**, 583–589 (2021).

66. Pettersen, E. F. et al. UCSF Chimera-a visualization system for exploratory research and analysis. *J. Comput. Chem.* **25**, 1605–1612 (2004).

67. Emsley, P., Lohkamp, B., Scott, W. G. & Cowtan, K. Features and development of Coot. *Acta Crystallogr. D. Biol. Crystallogr.* **66**, 486–501 (2010).

68. McCoy, A. J. et al. Phaser crystallographic software. *J. Appl. Crystallogr.* **40**, 658–674 (2007).

69. Sugiyama, Y. et al. Sfrp1 and Sfrp2 are not involved in Wnt/β-catenin signal silencing during lens induction but are required for maintenance of Wnt/β-catenin signaling in lens epithelial cells. *Dev. Biol.* **384**, 181–193 (2013).

70. Ohkawara, B. & Niehrs, C. An ATF2-based luciferase reporter to monitor non-canonical Wnt signaling in xenopus embryos. *Dev. Dyn.* **240**, 188–194 (2011).

71. Zhu, X. et al. Aberrant TGF-β1 signaling activation by MAF underlies pathological lens growth in high myopia. *Nat. Commun.* **12**, 2102 (2021).

72. Wang, X. et al. MiR-22-3p inhibits fibrotic cataract through inactivation of HDAC6 and increase of α-tubulin acetylation. *Cell Prolif.* **53**, e12911 (2020).